ARTICLE

On the compatibility of single-cell microcarriers (nanovials) with microfluidic impedance cytometry

Received 00th January 20xx,
Accepted 00th January 20xx

DOI: 10.1039/x0xx00000x

Cristian Brandi,[a,§] Adele De Ninno,[b,§] Filippo Ruggiero,[b] Emanuele Limiti,[c] Franca Abbruzzese,[c] Marcella Trombetta,[d] Alberto Rainer,[c,e] Paolo Bisegna,[a] and Federica Caselli [a,*]

We investigate for the first time the compatibility of nanovials with microfluidic impedance cytometry (MIC). Nanovials are suspendable crescent-shaped single-cell microcarriers that enable specific cell adhesion, the creation of compartments for undisturbed cell growth and secretion, as well as protection against wall shear stress. MIC is a label-free single-cell technique that characterizes flowing cells based on their electrical fingerprints and it is especially targeted to cells that are naturally in suspension. Combining nanovial technology with MIC is intriguing as it would represent a robust framework for the electrical analysis of single adherent cells at high throughput. Here, as a proof-of-concept, we report the MIC analysis of mesenchymal stromal cells loaded in nanovials. The electrical analysis is supported by numerical simulations and validated by means of optical analysis. We demonstrate that the electrical diameter can discriminate among free cells, empty nanovials, cell-loaded nanovials, and clusters, thus grounding the foundation for the use of nanovials in MIC. Furthermore, we investigate the potentiality of MIC to assess the electrical phenotype of cells loaded in nanovials and we draw directions for future studies.

1 Introduction

Modern approaches to personalized and precision medicine call for effective technological solutions for single-cell analysis and sorting. These solutions can be obtained through microfluidic devices, which enable high-throughput analysis with minimal sample volume and feature various integrated modules performing different functions (lab-on-a-chip).

Among the techniques employing microfluidics for single-cell analysis, microfluidic impedance cytometry (MIC) shows the attractive feature of exploiting cell intrinsic biophysical properties, thereby avoiding any labelling step.[1–3] By means of multifrequency electrical impedance measurements, MIC measures the electrical phenotype of individual biological cells, which is related to cell type and status. MIC has been extensively used for the label-free characterization of mammalian cells, human pathogens, and plant cells, for applications including viability assessment[4–6], subpopulation distinction[7–10], antimicrobial susceptibility testing[11–14] and deformability assessment.[15,16] MIC has also been reported as a tool for the non-invasive monitoring of 3D cell cultures under continuous flow,[17,18] and impedance-based microfluidic sorters have been proposed for sorting cells upon their electrical phenotype[18–21]. Emerging developments of the technique include the use of AI-based approaches for the analysis of MIC data[1,22,23] and the use of MIC to enable sample preparation for single-cell mass spectrometry.[24]

In MIC, cells are suspended in a conductive fluid and pumped through a microchannel with an electrical sensing zone where they are interrogated one-by-one. Accordingly, the technique is especially targeted for cells that are naturally in suspension, like cells found in bodily fluids (e.g., blood, seminal fluid, and urine) or ambient water (e.g., microalgae). Adherent cells can be measured with MIC too, via trypsinization and suspension. However, in that case, cells are not in their natural state when the measurement occurs.

Recently, hydrogel-based microcarriers have emerged as promising tools to boost cell analysis workflows [25–29]. Liu et al.[25] reported self-orienting crescent-shape particles and demonstrated their use as micro-buckets to carry living cells. Di Carlo's group[26,27] introduced lab-on-a-particle systems called nanovials as sub-nanoliter single-cell containers with open cavities for performing functional high-throughput cell screening. Nanovials offer the possibility of functionalizing their internal surface to promote the adhesion of cells and molecules in a specific way and the capability of creating uniform compartments (dropicles[27]) to facilitate cell growth and undisturbed secretion of bioproducts. In addition, they improve cell viability thanks to the protection against external stressors (both chemical, like surfactants, and mechanical, like wall shear

[a.] Department of Civil Engineering and Computer Science, University of Rome Tor Vergata, Rome, Italy. E-mail: caselli@ing.uniroma2.it
[b.] Italian National Research Council - Institute for Photonics and Nanotechnologies (CNR - IFN), Rome, Italy.
[c.] Department of Engineering, Università Campus Bio-Medico di Roma, via Álvaro del Portillo, 21, 00128, Rome, Italy.
[d.] Department of Science and Technology for Sustainable Development and One Health, Università Campus Bio-Medico di Roma, via Álvaro del Portillo 21, 00128, Rome, Italy.
[e.] Fondazione Policlinico Universitario Campus Bio-Medico, via Álvaro del Portillo, 200, 00128, Rome, Italy
§These authors contributed equally to this work.
Electronic Supplementary Information (ESI) available. See DOI: 10.1039/x0xx00000x

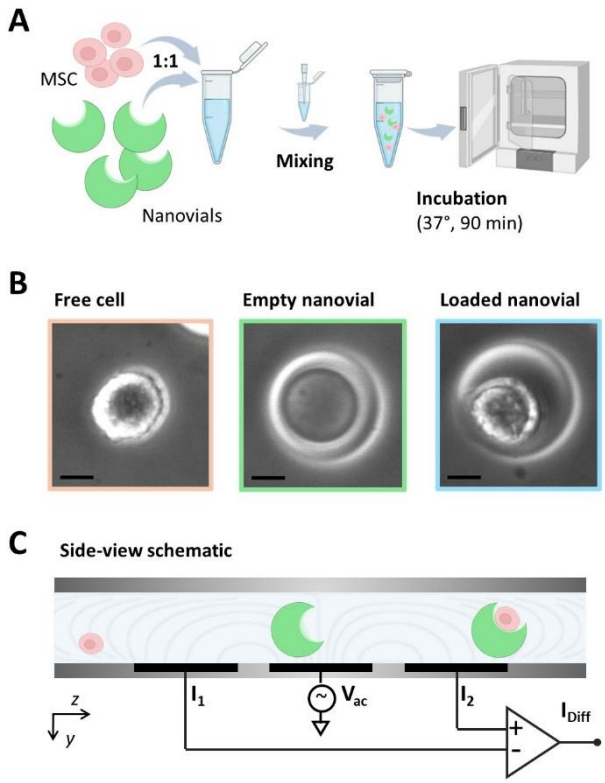

Fig. 1 (A) Illustration of the sample preparation protocol (MSC, mesenchymal stromal cells). (B) Representative microscopy images of a free cell, an empty nanovial, and a cell loaded nanovial (40 × objective, phase contrast, scale bar is 10 µm). (C) Schematic representation of the sensing zone of the impedance cytometer, comprising three coplanar electrodes on the bottom of the microchannel. The wiring scheme is also indicated: an AC voltage is applied to the central electrode and the differential current from the grounded lateral electrodes is acquired.

stress) and they are compatible with flow cytometry and single-cell sequencing instruments.[30–32] Several applications of nanovial technology have rapidly emerged, including sorting single T-cells based on secreted cytokines and surface marker[33], association of molecular signatures with antibody secretion in human plasma cells,[31] and combined analysis of growth-factor secretion and transcriptomes of mesenchymal stromal cells.[32]

This work aims to investigate, for the first time, the compatibility of nanovials with microfluidic impedance cytometry. Mesenchymal stromal cells are considered as a model of adherent cells in light of their therapeutic relevance,[34] and a simple impedance cytometry setup is used (Section 2). A suspension of cells and nanovials is incubated, to promote cell loading into nanovials, and then analysed with the impedance cytometer. The results of the electrical characterization (Section 3) are validated by means of synchronized image acquisition. It is shown that electrical signals at a single frequency can discriminate among free cells, empty nanovials, cell-loaded nanovials, and clusters, thus grounding the foundation for the use of nanovials in MIC. Furthermore, the potentiality of MIC to assess the electrical phenotype of cells loaded in nanovials is investigated in Section 4. Finally, a discussion about perspectives of the combination of nanovial technology and MIC is reported in Section 5, where we draw directions for future studies.

2 Materials and Methods

2.1 Microfluidic impedance chip

The microfluidic impedance chip was fabricated using standard microfabrication techniques, as previously reported.[35] The chip consists of a polydimethylsiloxane (PDMS) block containing the microfluidic channel, bonded to a glass slide with deposited Ti/Au microelectrodes (20 nm/200 nm). A three-electrode layout is considered, which has previously been validated by the authors for impedance measurements of red blood cells[36] and human cell lines.[6] To account for the larger dimensions of the nanovials (35 µm outer diameter), the chip dimensions were scaled up by a factor of three. Accordingly, the channel is 120 µm wide and 60 µm high; electrodes width in the flow direction is 90 µm, with a 30 µm spacing. A custom-built chip holder was used for fluidic and electric connections.

2.2 Sample preparation

Cells. Human mesenchymal stromal cells (Lonza, P5) were grown in α-MEM (Gibco) supplemented with 10% fetal bovine serum (Gibco) and 1% penicillin-streptomycin (Gibco). Upon subconfluence, cells were washed three times with phosphate-buffered saline (PBS) and then gently detached with TrypLE Express Enzyme (Thermo Fisher Scientific). Cells were resuspended in α-MEM at the concentration of 10^6 cells/mL.

Nanovials. Biotinylated nanovials (Partillion Bioscience) with 35 µm outer diameter and EZM™ formulation (i.e., cavity-localized extracellular matrix, ideal for adherent cells) were used. Prior to cell loading, 400k nanovials were washed in a washing buffer (PBS, 0.05% Pluronic F127, 0.5% bovine serum albumin) via centrifugation (200 × g, 5 minutes) and supernatant removal.

Cell loading into nanovials. The sample preparation protocol is illustrated in Fig. 1A. Cells and nanovials were mixed at a 1:1 ratio. Namely, 0.4 mL of cell suspension, containing 400k cells, were added to the washed nanovials (400k nanovials in 0.1 mL) in a 1.5 mL microcentrifuge tube. Cells and nanovials were gently mixed by pipetting. The microcentrifuge tube was incubated for 90 minutes at 37°C. To improve loading, the suspension was remixed by gentle pipetting after every 30 minutes. After incubation, a 5 µL droplet of suspension was observed under the microscope (Zeiss Axio Observer), confirming the presence of cell-loaded nanovials as well as free cells and empty nanovials (Fig. 1B). Clusters involving more than one nanovial and one cell were also found (e.g., two nanovials bound together by a cell, nanovials hosting more than one cell).

Sample dilution for impedance measurements. The sample was diluted (1:8) to obtain a theoretical nanovial concentration of 10^5 nanovials per mL. Two different dilution buffers were tested: (i) the washing buffer (1.3 S/m conductivity, 1 g/mL density) and (ii) the washing buffer supplemented with 13% (w/v) sucrose (0.9 S/m conductivity, 1.05 g/mL density) to mitigate particle sedimentation (nanovial density is about 1.1 g/mL).

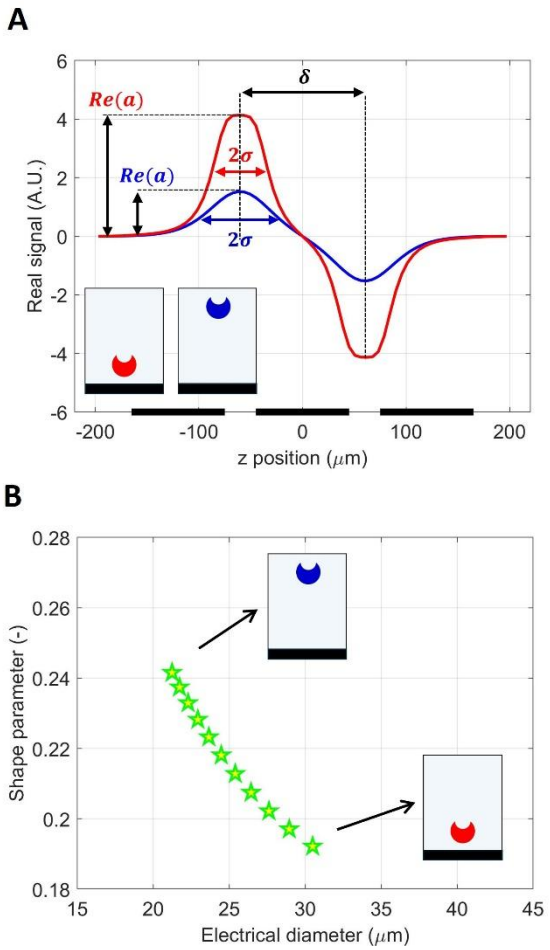

Fig. 2 In-silico analysis of position blurring. (A) Simulated differential current signals (real part) for empty nanovials traveling close to the electrodes or close to the ceiling (red and blue curve, respectively). (B) Simulated relationship between the shape parameter and the electrical diameter. Eleven equispaced vertical traveling positions are considered, assuming a minimum gap of 1.5 μm from channel floor/ceiling.

2.3 Experimental measurements

Impedance data acquisition and processing. The sample was injected into the microfluidic chip at 50 μL/min, by using a syringe pump (Elite 11, Harvard Apparatus). The chip, syringes and tubing were precoated with washing buffer before measurements. A schematic representation of the impedance measuring scheme is reported in Fig. 1C. AC voltage (4 V) at 0.5 MHz was applied at the central electrode, and the differential current through the grounded lateral electrodes was acquired using a standard impedance acquisition setting (HF2IS Zurich Instruments impedance spectroscope working at 115 kHz readout rate and 10 kHz bandwidth, following a HF2TA transimpedance amplifier with 10 kΩ gain).

The recorded impedance data streams were processed as described in previous works. Briefly, after a correlation-based event detection,[37] a bipolar Gaussian template was used for feature extraction.[6] The template is characterized by the following features (cf. Supplementary Material, Section S1): a complex amplitude a, a real peak-width control σ, and a real peak-to-peak time δ. The following metrics were considered in the analysis:

- the electrical diameter ($D = G|a|^{\frac{1}{3}}$, where G is a gain factor depending on the electronic circuitry) and the electrical phase (i.e., the phase of a),
- the shape parameter (i.e., σ/δ), which is a metric correlating with particle trajectory height,[35]
- the electrical velocity[36] ($v = L/\delta$, with $L = 120$ μm).

Synchronized video acquisition. Simultaneously to impedance measurements, the sample flowing through the sensing region was imaged with a high-speed camera (Photron, Mini UX100).[10] The frame rate was set to 2000 fps, with shutter time 30 μs. Synchronization of impedance data and video recordings was achieved via a hardware link, and the electrical velocity was used to estimate particle localization in the recorded images.

2.4 Finite element model

To assist the interpretation of the experimental design as well as to delineate guidelines for the development of MIC-tailored nanovials, we implemented a 3D finite element model of the microfluidic system[38,39] (cf. Section S2 of the Supplementary Material). The model includes the impedance chip and the cell-nanovial complex. As detailed in Section S3 of the Supplementary Material, an original parametric geometrical model of the cell-nanovial complex was developed, which is easily adaptable to mimic nanovials and cells of different sizes. Numerical simulations to investigate position blurring (Section 3.1, and Section S4 of the Supplementary Material) and orientation blurring (Section S5 of the Supplementary Material) were performed. Moreover, a parametric analysis elucidating the role of the nanovial dielectric properties (Section 4.1) as well as a numerical investigation of the potentiality of the methodology to assess cell viability (Section 4.3) were carried out.

3 Results

3.1 In-silico analysis of position blurring

In this study, we used a simple coplanar electrode design. Due to the non-uniformity of the electric field, this design exhibits position blurring,[40] i.e., identical particles traveling at different vertical positions produce different signals. Fig. 2A shows the simulated differential current signals for an empty nanovial traveling close to the electrodes (red curve) and for an identical empty nanovial traveling close to the channel ceiling (blue curve). The peak amplitude of the former is significantly higher than that of the latter. To cope with this issue, in a previous work[35] we demonstrated a mitigation strategy based on the so-called *shape parameter*, defined as the ratio between the pulse width σ and the peak-to-peak time δ. The shape parameter correlates with particle trajectory height. Hence, it can be used to correct the electrical diameter via calibration. Fig. 2B shows the electrical diameter and the shape parameter for nanovials traveling at eleven vertical positions: the shape parameter increases for increasing particle trajectory height, while the

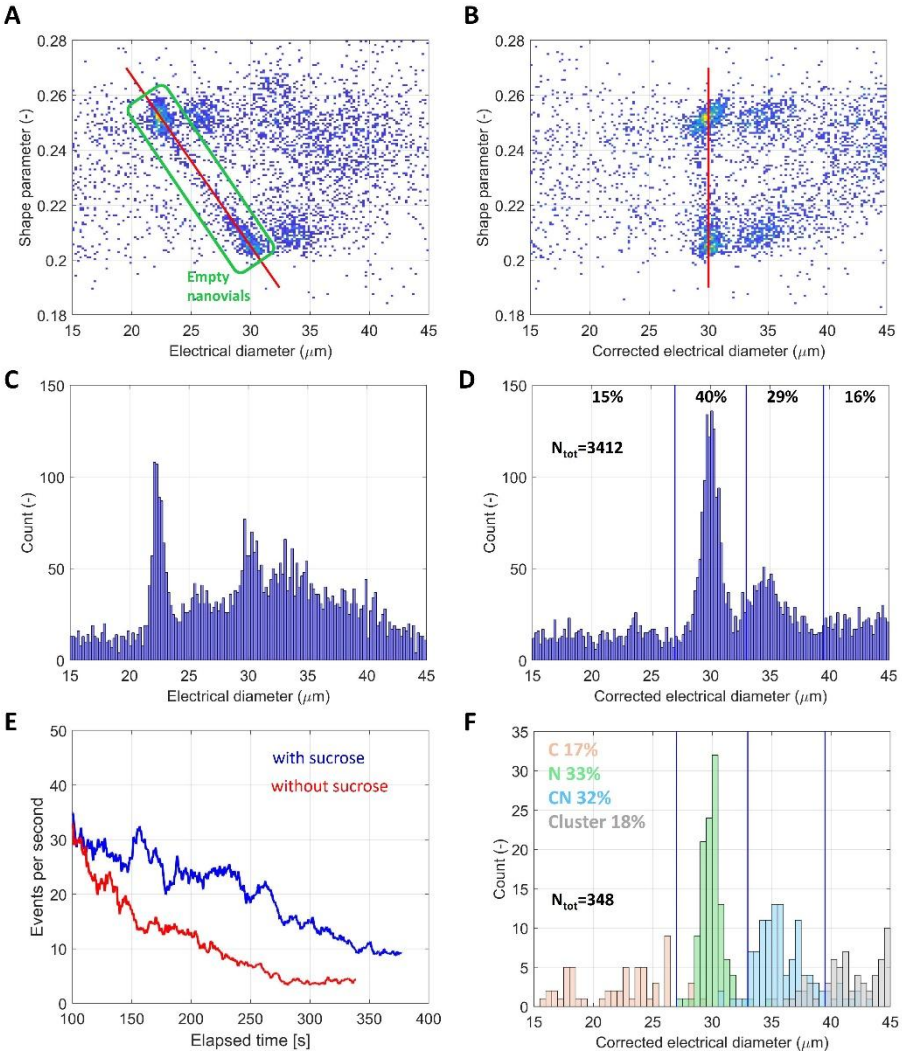

Fig. 3 (A) Density plot of the shape parameter against the electrical diameter. The population of empty nanovials is highlighted with an enclosing green gate and its linear fit is shown in red. (B) Density plot of the shape parameter against the corrected electrical diameter. (C) and (D) Histogram of electrical diameter and corrected electrical diameter, respectively. In (D) gating thresholds are also indicated, along with the fraction of events falling in each interval (number of total events: N_{tot} = 3412). (E) Event rate vs time elapsed form syringe loading (blue curve). For comparison, the event rate of an experiment with a buffer without sucrose is also shown (red curve). (F) Histogram of the corrected electrical diameter relevant to the subset of 348 events for which simultaneous video recordings were available. Color-coded labelling into populations (C, free cells; N, empty nanovials; CN, cell-nanovial complexes; clusters) is reported, as achieved by visual inspection of optical data.

electrical diameter decreases (see also Section S4 of the Supplementary Material). As shown in Section 3.2, this behaviour is found in the experimental measurements, thus enabling the implementation of the mitigation procedure.[35]

3.2 Impedance measurements results

The recorded data streams exhibited a good signal-to-noise ratio (SNR). Typical values were 29 dB, 37 dB, and 41 dB, for free cells, empty nanovials, and cell-loaded nanovials, respectively. The shape of the event signals was a bipolar Gaussian, and the standard processing algorithms could be applied.

Fig. 3A and C show the 2D density plot of the shape parameter against the electrical diameter and the histogram of the electrical diameter, respectively (for the sample with sucrose-augmented buffer). While it is difficult to identify the different subpopulations in the histogram (Fig.3C), a clearer picture is seen in the 2D density plot (Fig. 3A). Specifically, as confirmed by the optical inspection of the synchronized video recording, the population of empty nanovials can be easily identified (green gate in Fig. 3A). A higher density of empty nanovials is noticed at low (around 0.205) and high (around 0.25) shape parameter values, due to inertial particle focusing at two preferential heights.[41,42] The relationship between the shape parameter and the electrical diameter of the empty nanovials can be described by a linear fit (red line in Fig. 3A):

$$D = c_1 + c_2\left(\frac{\sigma}{\delta}\right), \quad (1)$$

with $c_1 = 63$ μm and $c_2 = -161$ μm. Such calibration coefficients, obtained on the empty nanovial population, can be used to correct the electrical diameter of the whole sample[6,35]. Specifically, the corrected electrical diameter is obtained as follows:

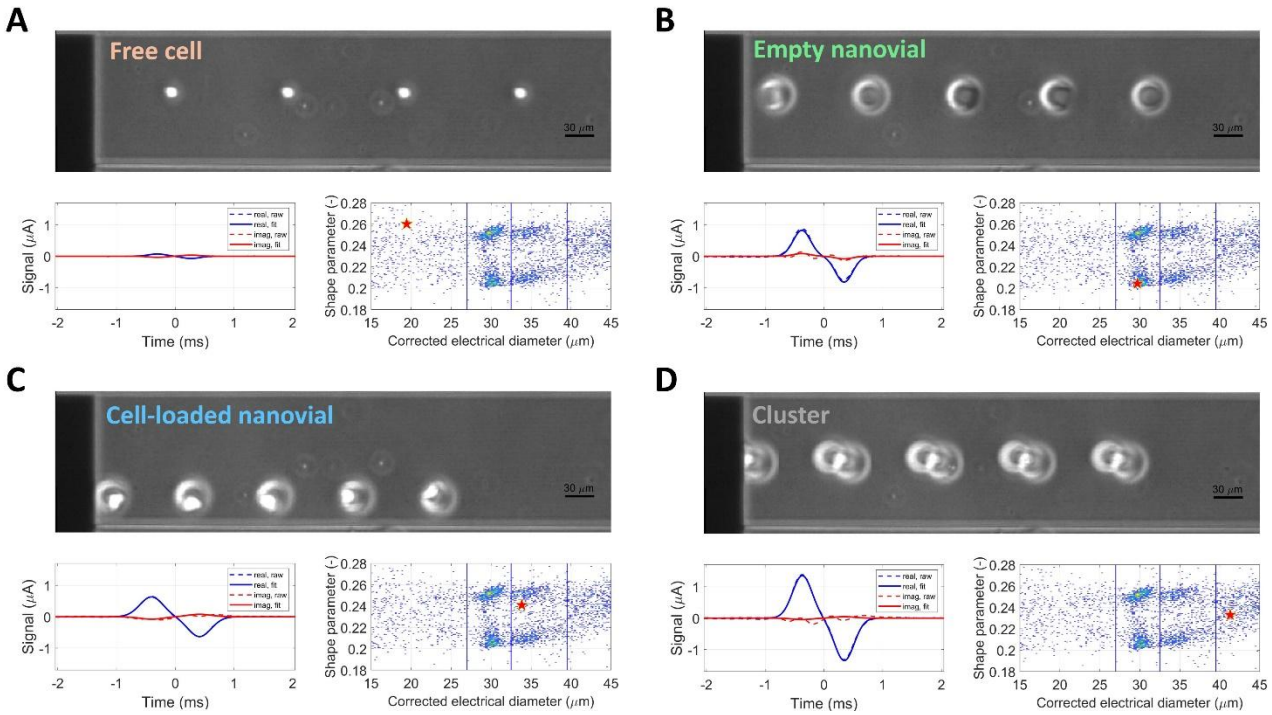

Fig. 4 Gallery of representative events, one for each subpopulation: (A) free cell, (B) empty nanovial, (C) cell-loaded nanovial, and (D) cluster. For each event, an overlay of consecutive snapshots is visualized (the dark band on the left is the last electrode of the sensing zone). The raw electrical signals (dotted lines) and their fit (continuous lines) are also shown (real part in red, imaginary part in blue), along with the data point localization (red star) in the density plot of the shape parameter against the corrected electrical diameter.

$$D\text{-corr} = \frac{D}{c_1 + c_2\left(\frac{\sigma}{\delta}\right)} D_{\text{ref}}, \qquad (2)$$

where $D_{\text{ref}} = 30$ μm is the diameter of a sphere isovolumic with the empty nanovial (which has a volume of 14500 μm³, as computed based on the geometric model described in Section S3 of the Supplementary Material). Fig. 3B and D show the 2D density plot of the shape parameter against the corrected electrical diameter and the histogram of the corrected electrical diameter, respectively. As expected, after correction for position blurring, the empty nanovial population is distributed around 30 μm in the histogram of Fig. 3D. The width of the distribution arises from intrinsic nanovial size heterogeneity and possible orientation effects. Another population distributed around 34.5 μm is found as well as data points at higher corrected electrical diameters. Furthermore, data points at the left of the empty nanovial populations are found.

The corrected electrical diameter is an accurate metric for particle size. Accordingly, the population around 34.5 μm reasonably represents cell-loaded nanovials, while the data points at larger diameters represents clusters comprising more than one cell and one nanovial. Similarly, the data points at the left of the empty nanovial population reasonably correspond to free cells. To confirm this interpretation, we analysed the synchronized video acquisitions (cf. Section 3.3).

A total of about 3400 electrical events were analysed. The measuring throughput (events per second) is reported in Fig. 3E (blue curve). It decreases over time, due to particle sedimentation.[30] This effect is exacerbated at lower buffer density, as shown by the quicker time decay of the event rate in case of buffer without sucrose (Fig. 3E, red curve). On the other hand, nanovial sedimentation is negligible during the measurement of each single event. In fact, according to Stokes' law, particle sedimentation velocity can be estimated as follows:

$$v_s = \frac{2(\rho_p - \rho_b) g r^2}{9\eta_b}, \qquad (3)$$

where ρ_p and ρ_b denote particle and buffer density, η_b denotes buffer viscosity (0.0015 Pa·s), g is the acceleration gravity, and r is particle radius. Accordingly, it turns out that v_s is about 16 μm/s. Since the event measurement time is about 2 ms (see traces in Fig. 4) the corresponding displacement is negligible with respect to channel height.

3.3 Optical validation

The images of about 350 events were analysed and labelled by inspection as free cells (C), empty nanovials (N), cell-loaded nanovials (CN) and clusters (clust). The histogram of the corrected electric diameter of these events is reported in Fig. 3F and confirms the previous interpretation. It was not possible to cross check all the 3400 electrical events with optical investigation, due to the memory limitation of the video acquisition system.

A representative event from each subpopulation (free cell, empty nanovial, cell-loaded nanovial, and cluster) is presented

in Fig. 4. For each event, an overlay of consecutive frames is shown, along with the raw and fitted impedance signals, and the position of the data point in the density plot of the shape parameter against the corrected electrical diameter. Furthermore, a video showing twenty events is included as Supplementary Material (Video S1). Nanovials were found to travel with different and varying orientations along the microchannel. Cells exhibited heterogeneous size and some cell clumps were found. In some cases, cells or cell clumps bonded together two or even three nanovials. The analysis of the clusters revealed a general increase of the corrected electrical diameter with the overall number of involved particles. The relative fractions of the four subpopulations were as follows: 17% free cells, 33% empty nanovials, 32% cell-loaded nanovials, 18% clusters. Accordingly, nanovials with single-cell occupancy are about 40% of all nanovials. Depending on the specific application and on the acceptable trade-off between the number of empty nanovials and clusters, different loading efficiency can be achieved by varying the cell-to-nanovial ratio during the incubation.

The optical analysis confirmed that the corrected electrical diameter $D\text{-corr}$ can be used to discriminate the four subpopulations. To this aim, the following gates were introduced (cf vertical blu lines in Fig. 3D and F):

- $15\ \mu\text{m} \leq D\text{-corr} < 27\ \mu\text{m}$, free cells
- $27\ \mu\text{m} \leq D\text{-corr} < 32.5\ \mu\text{m}$, empty nanovials
- $32.5\ \mu\text{m} \leq D\text{-corr} < 39.5\ \mu\text{m}$, cell-loaded nanovials
- $39.5\ \mu\text{m} \leq D\text{-corr} < 45\ \mu\text{m}$, clusters.

With these gates, the electrical classification (on all the electrical events) gave the following relative fractions: 15% free cells, 40% empty nanovials, 29% cell-loaded nanovials, 16% clusters, which are in good agreement with the relative fractions provided by the optical analysis (on a subset of events). Assuming the optical classification as the ground truth, the sensitivity and the positive predictive value (PPV) of the classification based on the corrected electrical diameter could be computed, for each subpopulation. The corresponding values are reported in Table 1, while the associated confusion matrix is shown in Fig. 5. Excellent classification results were obtained for free cells (91.5% sensitivity, 100% PPV) and empty nanovials (97.4% sensitivity, 93.3% PPV). Good results were obtained for cell-loaded nanovials (86.3% sensitivity, 85.6% PPV) and clusters (81.2% sensitivity, 81.5% PPV), with misclassification errors mainly associated to events composed by one nanovial and two cells or one nanovial and one large cell (see Section S6 of the Supplementary Material).

Table 1. Sensitivity and positive predictive value (PPV) of the electrical classification.

Subpopulation	Sensitivity (%)	PPV (%)
Free cells	91.5	100
Empty nanovials	97.4	93.3
Cell-loaded nanovials	86.3	85.6
Clusters	81.2	82.5

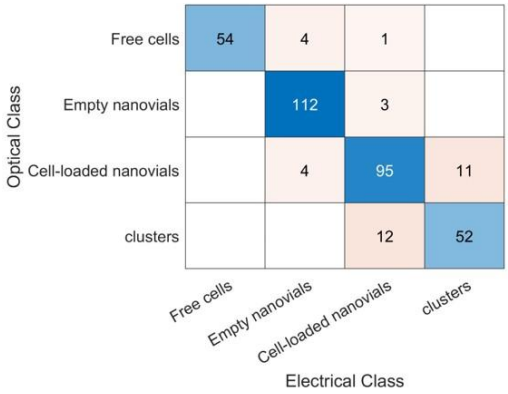

Fig. 5 Confusion matrix comparing the optical classification (assumed as ground truth) and the electrical classification.

4 Towards the characterization of cells loaded in nanovials

4.1 In-silico analysis of the role of nanovial conductivity

Several applications of microfluidic impedance cytometry of cells in suspension were reported in the last two decades[2]. Electrical fingerprints were able to discriminate different cell populations or cells at different states. Extending these results to cells adherent to nanovial cavities is challenging. A central aspect pertains the dielectric properties of the nanovial as compared to those of the medium. Ideally, if the nanovial has the same conductivity of the buffer (which is in the order of 1 S/m in impedance cytometry), the nanovial would be electrically invisible and, accordingly, all the functionalities demonstrated by MIC would be inherited. To elucidate this aspect, we carried on a parametric simulation study, varying the conductivity of the buffer (σ_b) and that of the nanovial (σ_n) in the range 0−1.5 S/m. Fig. 6A and B show the heatmaps of simulated peak signal (real part) for the empty and loaded nanovials, respectively. Larger signals are obtained when the nanovial is less conductive than the buffer (upper-right portion of the heatmaps). If the nanovial is isoconductive with the buffer (i.e., $\sigma_n = \sigma_b$), an empty nanovial is electrically invisible (cf. null diagonal entries in Fig. 6A). On the other hand, a non-null signal is measured for a cell-loaded nanovial. In this case the contrast – defined as the absolute relative difference between the signal peaks of the cell-loaded and empty nanovial – tends to infinity (cf. diagonal entries in Fig. 6C). High contrast is also obtained at high σ_b and slightly different σ_n (Fig. 6C). From an application viewpoint, the ideal system is characterized by signals with high SNR, the possibility to detect empty nanovials, and significant contribution of the cell to the measured signal (i.e., high contrast). Accordingly, high buffer conductivity and slightly lower nanovial conductivity would be optimal.

4.2 Experimental characterization of nanovial conductivity

Nanovial conductivity can be experimentally estimated by comparing impedance signals of empty nanovials (S^{nano}) with

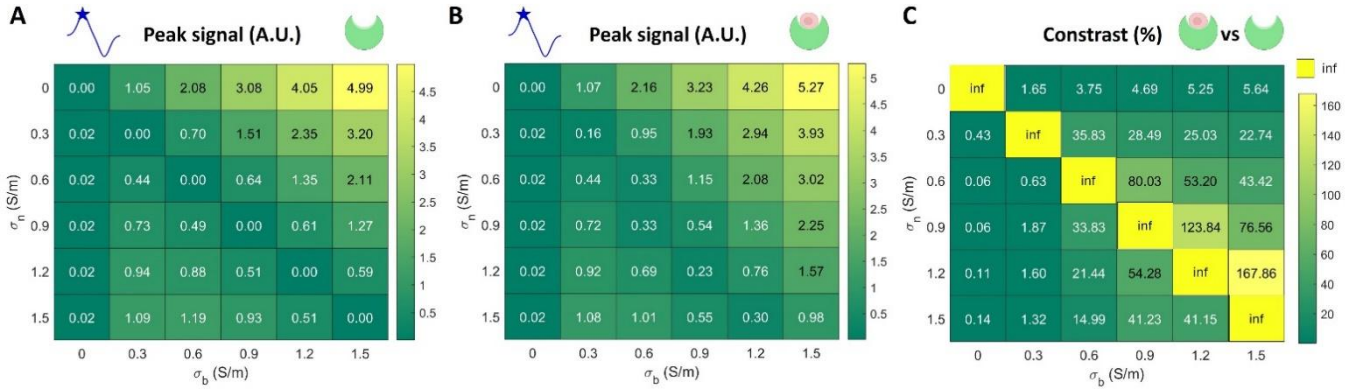

Fig. 6. In-silico parametric analysis of the role of nanovial and buffer conductivities, σ_n and σ_b, respectively. Heatmaps of the simulated peak signal for (A) an empty and (B) a cell-loaded nanovial, for conductivity values in the range 0–1.5 S/m. (C) Heatmap of the contrast between loaded and empty nanovials, defined as the absolute relative difference between their peak signals (in percentage).

impedance signals of reference beads (S^{beads}). In fact, the following relationship holds:

$$\frac{S^{\text{nanovial}}}{S^{\text{bead}}} = \frac{\tilde{f}_{\text{CM}}^{\text{nanovial}}}{\tilde{f}_{\text{CM}}^{\text{bead}}} \frac{V^{\text{nanovial}}}{V^{\text{bead}}}, \quad (4)$$

where $\tilde{f}_{\text{CM}}^{\text{nanovial}}$ and $\tilde{f}_{\text{CM}}^{\text{bead}}$ denote the Clausius-Mossotti factor of nanovials and beads, respectively, and V^{nanovial} and V^{bead} denote nanovial and bead volume, respectively (the reader is referred e.g. to Refs.[2,43] for the relevant theory). At low frequency, permittivities can be neglected and the Clausius-Mossotti factors become:

$$\tilde{f}_{\text{CM}}^{\text{nanovial}} \cong \frac{\sigma_n - \sigma_b}{\sigma_n + 2\sigma_b}, \quad \tilde{f}_{\text{CM}}^{\text{bead}} \cong -\frac{1}{2}, \quad (5)$$

(in the computation of $\tilde{f}_{\text{CM}}^{\text{bead}}$, bead conductivity has been neglected with respect to buffer conductivity). Hence, after simple math, equation (4) gives:

$$\sigma_n \cong \sigma_b \frac{2 - 2\alpha}{2 + \alpha}, \quad (6)$$

with:

$$\alpha = \left(\frac{S^{\text{nanovial}}}{S^{\text{bead}}}\right) \Big/ \left(\frac{V^{\text{nanovial}}}{V^{\text{bead}}}\right). \quad (7)$$

Figure 7 shows the histogram of the impedance signal for a mixed sample composed of empty nanovials and 20 µm diameter polystyrene beads. The histogram is well described by the sum of two Gaussian distributions with means 6.9 and 8.4. As verified by optical analysis of simultaneous video acquisitions, the left-hand distribution corresponds to the empty nanovial population whereas the right-hand distribution to the bead population. Hence, the ratio between S^{nanovial} and S^{beads} is 0.82. Since $V^{\text{nanovial}} = 14500$ µm³ and $V^{\text{bead}} = 4189$ µm³, it turns out that α =0.24 and therefore:

$$\sigma_n \cong 0.68\, \sigma_b = 0.6 \text{ S/m}. \quad (8)$$

Based on the analysis presented in section 4.1, the present experimental setting ($\sigma_b = 0.9$ S/m and $\sigma_n = 0.6$ S/m) is therefore promising for cell phenotyping applications.

4.3 Feasibility study of cell viability assessment

Loss of cell viability has been associated to alteration of cell membrane properties.[44,45] Necrotic cell death is accompanied by changes in the cell membrane permeability that are mirrored by an increase in the membrane conductance G_{mem}. Alterations of membrane capacitance C_{mem} have also been reported (e.g., during apoptosis), with a decrease in C_{mem} indicating a loss of membrane structures and the rounding of the cell membrane.[44] Since MIC is sensitive to membrane dielectric properties[6,7], we investigated its potential for assessing the viability of cells loaded in nanovials. Specifically, we simulated the impedance spectra of nanovials loaded with a reference cell, a cell with increased membrane conductance, or a cell with reduced membrane capacitance. The parameter values used in the simulation are reported in Table S1 of the Supplementary Material.

As shown in Fig. 8, nanovials housing cells with permeabilized membrane can be distinguished from nanovials housing intact cells due to their reduced electrical diameter at low frequency (0.5 MHz), which is however larger than the electrical diameter of empty nanovials. Moreover, while nanovials with intact cells exhibit negative phase shift with respect to empty nanovials, the electrical phase of nanovials housing cells with permeabilized membrane is analogous to that of empty nanovials. On the other hand, nanovials containing cells with reduced membrane capacitance exhibit an increased electrical diameter in the low frequency range and a membrane-capacitance relaxation taking place at higher frequency than nanovials with intact cells.

As a preliminary experimental verification, we performed an experiment with MSCs treated with Triton-X (0.01%) after incubation with nanovials. Triton-X is a non-ionic surfactant that is widely used to permeabilize eukaryotic cell membranes, thus increasing G_{mem}. As shown in Section S7 of the Supplementary Material, at 0.5 MHz the electrical diameter and the electrical phase of treated cells change compared to untreated cells in agreement with simulation results (i.e., reduced electrical diameter and electrical phase similar to that of empty nanovials).

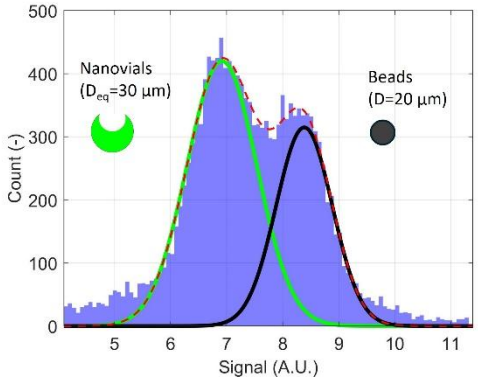

Fig. 7. Histogram of impedance signals (after compensation for position blurring) relevant to a mixture of empty nanovials and 20 µm polystyrene beads. Fitting Gaussian distributions are shown (green, empty nanovials; black, beads; red dashed, sum of the separate distributions).

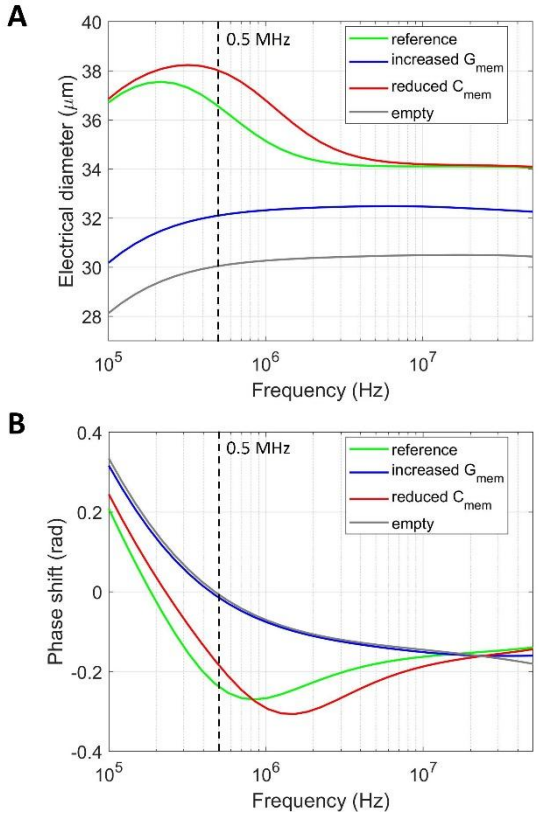

Fig. 8. Simulated impedance spectra of nanovials loaded with a reference cell (in green), a cell with increased membrane conductance (in blue), a cell with reduced membrane capacitance (in red), and empty nanovials (in gray). (A) Electrical diameter and (B) phase shift with respect to the phase of empty nanovials at 0.5 MHz.

5 Discussion & perspective

The possibility to combine nanovial technology with microfluidic impedance cytometry is very attractive as it represents an ideal framework for the electrical analysis of single adherent cells at high throughput. In this work, we explored such a possibility for the first time.

We exploited human mesenchymal stromal cells in combination with nanovials having an extracellular-matrix-coated cavity. Such formulation is tailored to facilitate cell loading, without the need for further functionalization. We used a straightforward cytometer design, based on three coplanar electrodes operated in a differential measurement scheme. We demonstrated that the electric diameter at 0.5 MHz can be used to distinguish among free cells, empty nanovials, cell-loaded nanovials, and clusters. To achieve this result, we exploited a strategy to compensate for positional dependence, based on the so-called shape parameter. As an alternative, a microfluidic chip with multiple facing electrode couples could be used, which is less sensitive to position blurring when operated in a proper measurement scheme.[43] However, this would require a more complex fabrication procedure. Emerging solutions based on wrap-around sensors can also be considered.[46]

Another point to consider is nanovial sedimentation, which was reported also in previous works using nanovials with standard fluorescence activated cell sorters.[30] We showed that by increasing the buffer density to 1.05 g/mL with sucrose supplementation, nanovial sedimentation was mitigated. This represents a trade-off value, as increasing the sucrose concentration above 13% (w/v) to achieve neutral buoyancy can be harmful to cells. Other buffer compositions could be investigated, e.g. based on Ficoll or Optiprep.[30] The latter could bring buffer density closer to nanovial density. On the other hand, the resulting buffer must preserve a sufficiently high conductivity, to obtain signals with good SNR, as well as a limited viscosity (to allow easy flow through the microfluidic chip). Working with neutrally buoyant nanovials would give a stable throughput over time. To increase the overall throughput, higher flow rates could be used (e.g., 100 or 150 µL/min) as well as higher concentration of nanovials (up to 3×10^5 per mL, unless tailored strategies for coincidence arbitration[22,36] are implemented).

Thanks to its sensitivity to size, MIC could be used for label-free monitoring of cell aggregates [47,48] or cell growth into nanovials. Moreover, the feasibility study presented in section 4.3, encourages future works using MIC for label-free viability assessment of cells loaded in nanovials. Also, optimization of nanovial production processes and cell-loading protocols may benefit from MIC as a tool for easy and fast characterization. Furthermore, microfluidic impedance-based sorting systems[19–21] could be used in combination with nanovial technology to enrich specific cell populations. In fact, nanovial cavities could be functionalized to facilitate attachment of selected cell subpopulations. Carrying adherent cells in nanovials can facilitate repeated measurements over time (e.g., for continuous online monitoring).

Novel formulations could be sought to further increase nanovial conductivity. The development of conductive hydrogels and polymers is presently an active research field,[49–53] offering promising opportunities for the development of MIC-tailored nanovials. Incidentally, PicoShells[54] are another lab-on-a-particle system that could be explored in combination with MIC. Picoshells have a porous PEG-based outer shell, which is permissive for solution exchange and, therefore, are

conductive. On the other hand, PicoShells are larger (90 µm diameter) than nanovials and they are not off-the-shelf available, as they are formed during the cell encapsulation phase.

Finally, MIC analysis could be integrated within the cell analysis workflows that leverage nanovial technology (analysis of surface markers, secretions, and transcriptome), as a further characterization step based on biophysical properties. In this way, an unprecedented multiparametric single-cell characterization could be achieved, with potential applications to cell therapy, monoclonal antibody-based drug discovery, and biomanufacturing processing.

Author Contributions

Conceptualization: F.C.; Methodology: F.C., C.B., A.D.N., A.R., P.B.; Software: P.B., F.C.; Formal Analysis: F.C.; Investigation: C.B., A.D.N., F.C., F.R., E.L., F.A.; Resources: F.C., A.D.N., A.R., P.B., M.T.; Data Curation: F.C.; Writing - Original Draft: F.C.; Writing - Review & Editing: P.B., A.R., C.B., A.D.N.; Visualization: F.C., C.B.; Supervision: F.C., A.D.N., A.R.; Project administration: F.C.; Funding acquisition: F.C., A.D.N., A.R.

Conflicts of interest

There are no conflicts to declare.

Acknowledgements

This work was supported by the Italian Ministry of University and Research under the PRIN 2022 programme (MIC-AIM project, grant 2022245PTX) funded by the European Union – Next Generation EU, Mission 4, Component 1 – CUP E53D23002530006. A.D.N., M.T., and A.R. acknowledge the Innovation Ecosystem Rome Technopole ECS00000024, funded by the European Union - Next Generation EU, PNRR Mission 4 Component 2 Investment 1.5.

References

1 T. Tang, T. Julian, D. Ma, Y. Yang, M. Li, Y. Hosokawa and Y. Yalikun, *Anal Chim Acta*, 2023, 1269.

2 C. Honrado, P. Bisegna, N. S. Swami and F. Caselli, *Lab Chip*, 2021, **21**, 22–54.

3 S. Zhu, X. Zhang, Z. Zhou, Y. Han, N. Xiang and Z. Ni, *Talanta*, 2021, 233.

4 J. Zhong, D. Yang, Y. Zhou, M. Liang and Y. Ai, *Analyst*, 2021, **146**, 1848–1858.

5 C. V. Bertelsen, G. E. Skands, M. González Díaz, M. Dimaki and W. E. Svendsen, *ACS Omega*, 2023, **8**, 7714–7721.

6 A. De Ninno, R. Reale, A. Giovinazzo, F. R. Bertani, L. Businaro, P. Bisegna, C. Matteucci and F. Caselli, *Biosens Bioelectron*, 2020, **150**, 111887.

7 C. Honrado, A. Salahi, S. J. Adair, J. H. Moore, T. W. Bauer and N. S. Swami, *Lab Chip*, 2022.

8 D. S. de Bruijn, P. M. ter Braak, D. B. Van de Waal, W. Olthuis and A. van den Berg, *Biosens Bioelectron*, 2021, **173**, 112808.

9 S. A. Kruit, D. S. de Bruijn, M. L. W. J. Broekhuijse, W. Olthuis and L. I. Segerink, *Biosensors (Basel)*, 2022, **12**, 679.

10 M. DaOrazio, R. Reale, A. De Ninno, M. A. Brighetti, A. Mencattini, L. Businaro, E. Martinelli, P. Bisegna, A. Travaglini and F. Caselli, *IEEE Trans Biomed Eng*, 2022, **69**, 921–931.

11 C. Troiano, A. De Ninno, B. Casciaro, F. Riccitelli, Y. Park, L. Businaro, R. Massoud, M. L. Mangoni, P. Bisegna, L. Stella and F. Caselli, *ACS Sens*, 2023, **8**, 2572–2582.

12 T. Tang, X. Liu, Y. Yuan, R. Kiya, T. Zhang, Y. Yang, S. Suetsugu, Y. Yamazaki, N. Ota, K. Yamamoto, H. Kamikubo, Y. Tanaka, M. Li, Y. Hosokawa and Y. Yalikun, *Sens Actuators B Chem*, 2023, **374**, 132698.

13 D. C. Spencer, T. F. Paton, K. T. Mulroney, T. J. J. Inglis, J. M. Sutton and H. Morgan, *Nat Commun*, 2020, **11**, 5328.

14 J. Chen, J. Zhong, Y. Chang, Y. Zhou, S. H. Koo, T. Y. Tan, H. Lei and Y. Ai, *Small*, 2023, **n/a**, 2303352.

15 R. Reale, A. De Ninno, T. Nepi, P. Bisegna and F. Caselli, *IEEE Trans Biomed Eng*, 2022, 1–9.

16 C. Petchakup, H. Yang, L. Gong, L. He, H. M. Tay, R. Dalan, A. J. Chung, K. H. H. Li and H. W. Hou, *Small*, 2022, **18**, 2104822.

17 L. Gong, C. Petchakup, P. Shi, P. L. Tan, L. P. Tan, C. Y. Tay and H. W. Hou, *Small*, 2021, **17**, 2007500.

18 L. Gong, L. He, N. Lu, C. Petchakup, K. H. H. Li, C. Y. Tay and H. W. Hou, *Adv Healthc Mater*, **n/a**, 2304529.

19 P. Li and Y. Ai, *Anal Chem*, 2021, **93**, 4108–4117.

20 J. Zhong, M. Liang, Q. Tang and Y. Ai, *Mater Today Bio*, 2023, **19**, 100594.

21 B. de Wagenaar, S. Dekker, H. L. de Boer, J. G. Bomer, W. Olthuis, A. Van Den Berg and L. I. Segerink, *Lab Chip*, 2016, **16**, 1514–1522.

22 F. Caselli, R. Reale, A. De Ninno, D. Spencer, H. Morgan and P. Bisegna, *Lab Chip*, 2022, **22**, 1714–1722.

23 Y. Feng, Z. Cheng, H. Chai, W. He, W. Wang, L. Huang and W. Wang, *Lab Chip*, 2021.

24 J. Zhu, S. Pan, H. Chai, P. Zhao, Y. Feng, Z. Cheng, S. Zhang and W. Wang, *Small*, **n/a**, 2310700.

25 Q. Liu, M. Zhao, S. Mytnyk, B. Klemm, K. Zhang, Y. Wang, D. Yan, E. Mendes and J. H. van Esch, *Angewandte Chemie*, 2019, **131**, 557–561.

26 S. Lee, J. de Rutte, R. Dimatteo, D. Koo and D. Di Carlo, *ACS Nano*, 2022, **16**, 38–49.

27 J. de Rutte, R. Dimatteo, M. M. Archang, M. van Zee, D. Koo, S. Lee, A. C. Sharrow, P. J. Krohl, M. Mellody, S. Zhu, J. V. Eichenbaum, M. Kizerwetter, S. Udani, K. Ha, R. C. Willson, A. L. Bertozzi, J. B. Spangler, R. Damoiseaux and D. Di Carlo, *ACS Nano*, 2022, **16**, 7242–7257.

28 Y. Yang, S. I. Vagin, B. Rieger and G. Destgeer, *bioRxiv*, 2023, 2023.10.06.561257.

29 H. Miwa, R. Dimatteo, J. de Rutte, R. Ghosh and D. Di Carlo, *Microsyst Nanoeng*, 2022, **8**, 84.

30 J. de Rutte, R. Dimatteo, S. Zhu, M. M. Archang and D. Di Carlo, *SLAS Technol*, 2022, **27**, 150–159.

31 R. Y.-H. Cheng, J. de Rutte, C. E. K. Ito, A. R. Ott, L. Bosler, W.-Y. Kuo, J. Liang, B. E. Hall, D. J. Rawlings, D. Di Carlo and R. G. James, *Nat Commun*, 2023, **14**, 3567.

32 S. Udani, J. Langerman, D. Koo, S. Baghdasarian, B. Cheng, S. Kang, C. Soemardy, J. de Rutte, K. Plath and D. Di Carlo, *Nat Nanotechnol*, , DOI:10.1038/s41565-023-01560-7.

33 D. Koo, R. Dimatteo, S. Lee, J. de Rutte and D. Di Carlo, *bioRxiv*, , DOI:10.1101/2022.04.28.489940.

34 M. F. Pittenger, D. E. Discher, B. M. Péault, D. G. Phinney, J. M. Hare and A. I. Caplan, *NPJ Regen Med*, 2019, 4.

35 V. Errico, A. De Ninno, F. R. Bertani, L. Businaro, P. Bisegna and F. Caselli, *Sens Actuators B Chem*, 2017, **247**, 580–586.

36 F. Caselli, A. De Ninno, R. Reale, L. Businaro and P. Bisegna, *IEEE Trans Biomed Eng*, 2020, **68**, 340–349.

37 F. Caselli and P. Bisegna, *IEEE Trans Biomed Eng*, 2016, **63**, 415–422.

38 F. Caselli and P. Bisegna, *Med Eng Phys*, 2017, **48**, 81–89.

39 F. Caselli, P. Bisegna and F. Maceri, *Journal of Microelectromechanical Systems*, 2010, **19**, 1029–1040.

40 H. Daguerre, M. Solsona, J. Cottet, M. Gauthier, P. Renaud and A. Bolopion, *Lab Chip*, 2020, **20**, 3665–3689.

41 D. Di Carlo and D. Di Carlo, *Lab Chip*, 2009, **9**, 3038–3046.

42 R. Reale, A. De Ninno, L. Businaro, P. Bisegna and F. Caselli, *Microfluid Nanofluidics*, 2018, **22**, 1–13.

43 D. Spencer and H. Morgan, *ACS Sens*, 2020, **5**, 423–430.

44 P. Patel and G. H. Markx, *Enzyme Microb Technol*, 2008, 43.

45 X. Wang, F. F. Becker and P. R. C. Gascoyne, *Biochim Biophys Acta*, 2002, **1564**, 412–420.

46 O. Civelekoglu, R. Liu, N. Asmare, A. K. M. Arifuzzman and A. F. Sarioglu, *Sens Actuators B Chem*, 2023, **375**, 132874.

47 K. Torres-Castro, M. S. Azimi, W. B. Varhue, C. Honrado, S. M. Peirce and N. S. Swami, *Analyst*, , DOI:10.1039/d2an00222a.

48 N. Sethia, J. S. Rao, Z. Khashim, A. M. R. Schornack, M. L. Etheridge, Q. P. Peterson, E. B. Finger, J. C. Bischof and C. S. Dutcher, *Langmuir*, 2024, **40**, 3453–3462.

49 B. Khan, S. Abdullah and S. Khan, *Micromachines (Basel)*, 2023, 14.

50 G. Kougkolos, M. Golzio, L. Laudebat, Z. Valdez-Nava and E. Flahaut, *J Mater Chem B*, 2023, 11, 2036–2062.

51 K. Liu, S. Wei, L. Song, H. Liu and T. Wang, *J Agric Food Chem*, 2020, 68, 7269–7280.

52 S. D. Kim, K. Kim and M. Shin, *Nano Converg*, 2023, 10.

53 A. De Masi, P. L. Scognamiglio, E. Battista, P. A. Netti and F. Causa, *J Mater Chem B*, 2022, **10**, 1980–1990.

54 M. van Zee, J. de Rutte, R. Rumyan, C. Williamson, T. Burnes, R. Radakovits, A. Sonico Eugenio, S. Badih, S. Lee, D.-H. Lee, M. Archang and D. Di Carlo, *Proceedings of the National Academy of Sciences*, 2022, **119**, e2109430119.